

Carbon xerogel-enhanced microchannel-structured beads for organic pollutants degradation: A novel catalyst for synergistic microscale process intensification

Jiaojiao Zheng^a, Francisco R. García-García^b, Yang Yang^c , Kang Li^d, Tony Bridgwater^a, Haiping Yang^c, Zhentao Wu^{a,*} 

^a Energy and Bioproducts Research Institute (EBRI), Aston University, Birmingham B4 7ET, UK

^b The University of Edinburgh, School of Engineering, Institute for Materials and Processes, Sanderson Building, The King's Buildings, Mayfield Road, Edinburgh, Scotland EH9 3JL, UK

^c State Key Laboratory of Coal Combustion, School of Energy and Power Engineering, Huazhong University of Science and Technology, Wuhan 430074, China

^d Barrer Centre, Department of Chemical Engineering, Imperial College London, London SW7 2AZ, UK

ARTICLE INFO

Keywords:

Microchannel-structured beads
Diffusional transfer
Process intensification
Carbon xerogel
Advanced oxidation processes

ABSTRACT

A novel carbon xerogel-enhanced microchannel-structured alumina bead (3 mm in diameter, ACXx) was developed to enhance organic pollutant degradation in peroxymonosulfate (PMS)-activated advanced oxidation processes (AOPs). This catalyst design uniquely combines microstructure-enhanced diffusional transfer with material synergies. Cobalt-based active phases impregnated into a mesoporous carbon coating, prepared via sol-gel methods, increased the alumina bead's specific surface area by 14-fold, improving dispersion of 2 wt% Co₃O₄ (2Co/ACXx). The carbon coating provided complementary adsorptive and catalytic properties, significantly outperforming alumina beads lacking these synergies (e.g., those coated with mesoporous γ -Al₂O₃) or the pristine alumina bead, which relies solely on diffusional mass transfer through its bimodal pore structure. This study highlights the synergistic benefits of microstructural optimization and functional material integration in advancing heterogeneous catalytic efficiency. The approach offers a versatile framework for designing high-performance catalysts for AOPs and other applications requiring intensified mass transfer and reaction kinetics at microscales.

1. Introduction

In many industrial processes involving heterogeneous reaction systems, chemical reactions are limited by mass or heat transfer rather than reaction kinetics [1]. In mass transfer-controlled reactions, the reaction rate is typically determined by how quickly reactants reach the reactive sites, often limited by slow diffusion at microscales or inadequate mixing in the bulk phase. Process intensification (PI) techniques are explored to address these limitations by, for example, configuring reactions within small channels, shortening diffusional distances, and thereby enhancing reactant diffusion efficiency [2,3]. However, the small and narrow internal channel sizes (approximately 0.01–1 mm in diameter) of microreactors result in a high pressure drop as fluids pass through [4].

One potential solution to this challenge involves millimetre-scale structured catalyst substrates, such as monolithic substrates and

ceramic foam supports [5,6]. For example, it has been reported that the Fe/SiC honeycomb monolithic reactor [7] and ZSM-5@ceramic foam catalysts [5] demonstrated superior catalytic performance compared to the slurry reactor and ZSM-5 powder, respectively. Additionally, the external mass transfer coefficients for the conventional ceramic beads (1.5 mm and 3 mm in diameter), honeycombs (400 cells per square inch (CPSI)) and ceramic foams (20 pores per inch (PPI) and 45 PPI) followed a definite trend, with the ranking order of 1.5 mm beads >> 45 PPI foams > 20 PPI foams \approx 3.3 mm beads > 400 CPSI honeycombs [8]. Meanwhile, the pressure drop was ranked in the following order: 1.5 mm beads > 3.3 mm beads \approx 45 PPI foams \approx 20 PPI foams > 400 CPSI honeycombs.

Technically, conventional ceramic bead with a uniform macroscopic catalyst distribution (homo-type) suffers from a severe mass transfer resistance, as reactants need to travel long diffusional paths from the

* Corresponding author.

E-mail address: z.wu7@aston.ac.uk (Z. Wu).

<https://doi.org/10.1016/j.apcatb.2025.125069>

Received 8 October 2024; Received in revised form 12 January 2025; Accepted 14 January 2025

Available online 15 January 2025

0926-3373/© 2025 The Authors. Published by Elsevier B.V. This is an open access article under the CC BY license (<http://creativecommons.org/licenses/by/4.0/>).

bulk fluids to access the reactive catalytic sites within the inner cores. Given its decent mass transfer coefficients and pressure drop compared to other catalyst substrates, it holds tremendous prospects for microscale PI technology if innovation is embraced. In our recent work, an innovative microchannel-structured ceramic bead (3 mm in diameter) with radial finger-like microchannels (20–100 μm in width) was developed for the first time to decouple structural limitations of catalyst design [9]. These unique beads possess both large pores (micrometre-sized microchannels) and small pores (nanometre-sized clusters of alumina granules), with large pores overcoming the mass transfer resistance by prompt transportation of large molecules, and small pores contributing to dispersing more catalytic active phase. Simultaneously, the large size of ceramic beads can also maintain a steady low pressure drop [10]. However, the low specific surface area ($S_{\text{BET}} = 3.65 \text{ m}^2/\text{g}$) of these beads suffered from catalyst agglomeration, even with a cobalt loading of 5 wt % [9].

Building on this finding, we sought to integrate high-surface-area materials into the microchannels of the beads to enhance their practical applicability. High-surface-area carbonaceous materials, such as activated carbons [11,12], carbon nanotubes [13], and carbon xerogels (CXs) [11,14], present a promising option. Among these, carbon xerogels are particularly noteworthy as they can be produced using the sol-gel method [11,15], which is crucial for incorporating carbon into the beads. As an efficient reaction system, peroxymonosulfate (PMS)-activated advanced oxidation processes (AOPs) can generate highly reactive species, such as $\text{SO}_4^{\cdot-}$ and $\cdot\text{OH}$, to degrade and mineralise organic pollutants [16]. In AOPs, carbon materials also exhibited remarkable adsorption capacity [14,17], and carbon materials with oxygen-containing functional groups, particularly the $\text{C}=\text{O}$, were favourable to PMS activation [18–20], potentially contributing to a synergistic effect towards AOPs reactions. This would streamline multiple operational units/equipment and process tasks into a single multifunctional alumina bead, fulfilling another crucial principle of the PI technology [21,22], thereby achieving synergistic process intensification at microscale process unit.

As a result, PMS-activated AOPs will be applied as the model reaction system in this work to validate the microstructural advantages of novel modified microchannel-structured alumina beads (ACXx). For comparison, the most commonly used washcoat, $\gamma\text{-Al}_2\text{O}_3$, was also applied (A ($\gamma\text{-Al}_2\text{O}_3$)). After incorporating with cobalt-based catalyst (2Co/ACXx), we will systematically investigate the influences of specific surface area, washcoating properties (carbon xerogels and $\gamma\text{-Al}_2\text{O}_3$), sulfamethoxazole concentrations (10 mg/L, 20 mg/L, 40 mg/L), reaction temperatures (20 $^\circ\text{C}$, 30 $^\circ\text{C}$, 40 $^\circ\text{C}$), catalyst dosage, and organic pollutant types - type I: PPCPs (sulfamethoxazole); type II: phenols (4-hydroxybenzoic acid and phenol); type III: dyes (methyl orange) - on the catalytic performance. Furthermore, we will examine the catalytic mechanism of 2Co/ACXx/PMS system, as well as its stability and reusability.

2. Materials and methods

2.1. Materials

Resorcinol (ACS reagent, $\geq 99\%$), formaldehyde (ACS reagent, 37 wt% sol.), sodium carbonate (BioXtra, $\geq 99\%$), Oxone® (PMS, $\text{KHSO}_5 \cdot 0.5\text{KHSO}_4 \cdot 0.5\text{K}_2\text{SO}_4$), sulfamethoxazole (SMX), 4-hydroxybenzoic acid (p-HBA), phenol, p-benzoquinone (p-BQ, $\geq 98\%$), tert-butanol (tBA, $\geq 99.5\%$), sodium azide (NaN_3 , $\geq 99.5\%$), methyl orange (MO, ACS reagent), and acetic acid (ReagentPlus®, $\geq 99\%$) were all obtained from Sigma-Aldrich. Cobalt nitrate hexahydrate ($\text{Co}(\text{NO}_3)_2 \cdot 6\text{H}_2\text{O}$, 99% pure), methanol (HPLC grade, $\geq 99.8\%$), and nitric acid (HNO_3 , analytical reagent grade, 70%) were purchased from Fisher Scientific. All chemicals were used as received without any further purification. Milli-Q water (18.3 $\text{M}\Omega \text{ cm}$ at 25 $^\circ\text{C}$) was used during the whole experimental process.

2.2. Preparation of carbon xerogel-based alumina beads (ACXx)

Microchannel-structured alumina beads (ACX0) of approximately 3 mm in diameter were prepared by a phase-inversion and sintering-assisted method, as reported in our previous work [9]. Prior to the dip coating process, carbon xerogels, labelled as CX, were prepared by a sol-gel method [11]. Specifically, a precursor solution of resorcinol (R), formaldehyde (F) and sodium carbonate (C) with molar ratios of $\text{R/C} = 200$ and $\text{R/F} = 0.5$ were mixed and stirred for 30 min. The starting solution was named as CX1, and then it was mixed with DI water to produce the rest of CXx sols and x hereafter refers to the CX solution concentrations. The volume ratios of starting solution (CX1) to the top up DI water for CX2, CX3 and CX4 were set as 4:1, 4:2, and 4:3, respectively.

Afterwards, the microchannel-structured alumina beads were immersed in four CXx sol solutions for 10 min, then dried at 65 $^\circ\text{C}$ for 20 min in a rotavapor (Buchi), and gelled at 100 $^\circ\text{C}$ in an oven overnight. The dried samples were then sintered at 800 $^\circ\text{C}$ for 1 h in a nitrogen atmosphere with a heating rate of 5 $^\circ\text{C}/\text{min}$ to carbonize the carbon xerogel gels inside the beads. The prepared CXx-based alumina beads were labelled as ACXx ($x = 0, 1, 2, 3, 4$). The schematic diagram of the synthesis of ACXx samples was presented in Fig. S1. For comparison, CX powder was prepared using the same approach without the addition of alumina beads; Another sample A($\gamma\text{-Al}_2\text{O}_3$) prepared by sol-gel method [23] was also prepared for reference.

2.3. Incorporation of Co-based catalysts (2Co/ACXx)

2 wt% of cobalt oxide was incorporated on the ACXx beads, including ACX0 without carbon xerogel loadings, by the traditional incipient wetness impregnation method [9]. Firstly, 0.74 g of cobalt nitrate hexahydrate was dissolved in 4.5 mL of DI water, and then slowly added to 10 g of ACXx beads, resulting in a Co_3O_4 to ACX weight ratio of 2 wt%. Then, the dried samples were sintered at 450 $^\circ\text{C}$ for 3 h in a flow of N_2 atmosphere (100 mL/min) at a heating rate of 5 $^\circ\text{C}/\text{min}$. These catalysts were denoted as 2Co/ACXx, where “x” refers to the CXx sol concentration, as previously illustrated. 2Co/A($\gamma\text{-Al}_2\text{O}_3$) was synthesised using the same impregnation method with an identical cobalt loading.

2.4. Characterisation

Powder X-ray diffraction (XRD) pattern of ACXx and 2Co/ACXx were recorded on an advanced X-ray diffractometer (Bruker D8, Germany), with $\text{Cu K}\alpha$ radiation ($\lambda = 1.5418 \text{ \AA}$), operated at 40 kV and 40 mA. The specific surface area of samples was obtained at $-196 \text{ }^\circ\text{C}$ with liquid nitrogen on a Nova 4000 porosimeter, using the Brunauer–Emmett–Teller (BET) method and the Barrett, Joyner, and Halenda (BJH) method. Prior to the measurement, samples were gently ramped to 130 $^\circ\text{C}$ and degassed under vacuum for 5–6 h. Thermogravimetric analysis (TGA) was carried out on the TGA-DSC 2 STAR system (Mettler Toledo) with a heating rate of 10 $^\circ\text{C}/\text{min}$ in either air or nitrogen atmosphere for different sample analysis. The morphology of all alumina beads before and after cobalt loading was analysed by a scanning electron microscopy (SEM, JEOL JSM-IT200, operating at 5 kV and working distance of 10 mm). The chemical states and compositions of alumina beads with (2Co/ACX1) and without (2Co/ACX0) carbon xerogel loadings were analysed by X-ray photoelectron spectroscopy (XPS, Thermo Scientific K-Alpha Photoelectron spectrometer, USA) using an Al $\text{K}\alpha$ source. All binding energies were calibrated by C 1s (284.8 eV). The cobalt content and metal leaching results were analysed by an inductively coupled plasma-optical emission spectrometry (ICP-OES) apparatus (iCAP 7000 Series).

2.5. Catalytic degradation of various organic pollutants in a PMS-activated system

The catalytic performance of 2Co/ACXx was evaluated for the degradation of organic pollutants (SMX, p-HBA, and phenol solutions) in a PMS activated system. The experiments were carried out in a batch reactor in a water bath and connected with a mechanical overhead stirrer. Initially, a predetermined amount of catalyst was added in 100 mL of pollutant solutions with vigorously stirring at 150 rpm for 30 min to achieve the adsorption-desorption equilibrium. Thereafter, the catalytic reactions were triggered by adding PMS (0.31 mM) and continued for another 120 min. When the reaction was in process, 1 mL of aqueous solution was withdrawn by a syringe at fixed time intervals and filtered by a 0.2 μm PTFE syringe filter, and then immediately injected into a HPLC vial with 0.5 mL methanol included as a quenching agent. The concentrations of SMX, p-HBA, and phenol solutions were all analysed on an ultra-high performance liquid chromatography (UHPLC, Shimadzu Prominence, Japan) using a UV detector set at 270 nm of wavelength [9,24,25]. A C-18 column (Restek Rapter, 2.7 μm , 100 \times 2.1 mm, France) was used to differentiate the organics. The mobile phase was composed of methanol and ultrapure water (pH 3.5 adjusted by acetic acid) with a volume ratio of 90:10 at a flowrate of 0.3 mL/min [26]. The catalytic degradation kinetics of three organic pollutants followed the pseudo-first-order kinetic model and can be estimated using the following equation [27]:

$$\ln\left(\frac{C}{C_0}\right) = -kt \quad (1)$$

where k is the apparent reaction rate constant (min^{-1}), and C_0 and C are the initial pollutant concentration (mg/L), and the pollutant concentration at specific time intervals (mg/L), respectively.

3. Results and discussion

3.1. XRD, BET and TGA analysis of ACXx and 2Co/ACXx samples

Fig. 1 shows the XRD patterns of the samples before and after CX and cobalt loadings. All ACXx samples in Fig. 1(a) demonstrated diffraction peaks corresponding to the $\alpha\text{-Al}_2\text{O}_3$ (JCPD file no. 88-0826) [9], and no diffraction signals of carbon xerogels could be observed. This might be attributed to the weak diffraction peaks for the pure CX powder owing to their intrinsic nature [28], as shown in Fig. 1(a–b). However, the presence of carbon xerogel in ACXx samples was evident due to the noticeable colour change after CX loadings, as shown in Fig. S1. Additional evidence will be provided in the following characterisation

results, including significant S_{BET} increase (Table 1), TGA results (Fig. 2), SEM images (Fig. 4) and XPS spectra (Fig. 5(d)). Likewise, no significant differences were observed in the XRD patterns for 2Co/ACXx samples after cobalt incorporation (Fig. 1(c)) compared to ACXx samples, which could be ascribed to the low Co content of 2 wt% and uniform distribution of Co on the alumina beads [9,27]. Furthermore, the detection of 1.72 wt% Co in 2Co/ACX1 sample through ICP measurement could validate the existence of cobalt.

Table 1 summarised the structural characteristics of three types of microchannel-structured alumina beads: (1) ACX0 (without any wash-coatings), (2) A($\gamma\text{-Al}_2\text{O}_3$) (with $\gamma\text{-Al}_2\text{O}_3$ washcoatings), and (3) ACXx (with carbon xerogel washcoatings) samples before and after cobalt impregnation. Apparently, the base ACX0 beads without any wash-coatings had the lowest BET surface area ($S_{\text{BET}} = 3.65 \text{ m}^2/\text{g}$). As dip coating with $\gamma\text{-Al}_2\text{O}_3$ sols, the specific surface area significantly increased to $36.03 \text{ m}^2/\text{g}$, which is 9.9 times higher than that of ACX0. When changed the coatings to carbon xerogel sols, the S_{BET} further increased, with $66.98 \text{ m}^2/\text{g}$, $59.92 \text{ m}^2/\text{g}$, $56.62 \text{ m}^2/\text{g}$, and $37.20 \text{ m}^2/\text{g}$ for ACX1, ACX2, ACX3 and ACX4, respectively. Herein, ACX1 sample with lowest water content possessed the highest surface area, which is 18.6 times and 1.9 times than those of ACX0 and A($\gamma\text{-Al}_2\text{O}_3$) samples. The N_2 adsorption-desorption isotherms in Fig. S2 (a) were consistent with the S_{BET} results, with all ACXx samples displaying a low but increasing adsorption capacity as carbon xerogel sol concentration rose. The increased specific surface area of CX and CX-based beads could be attributed to several factors during the synthesis process, as detailed in

Table 1

Textural properties of A($\gamma\text{-Al}_2\text{O}_3$) and ACXx samples before and after cobalt impregnation.

Sample	S_{BET} (m^2/g)	V_T (cc/g)	D_p (nm)
ACX0	3.65	0.01	/
A($\gamma\text{-Al}_2\text{O}_3$)	36.03	0.05	5.78
ACX1	66.98	0.05	3.15
ACX2	59.92	0.04	2.39
ACX3	56.62	0.04	2.59
ACX4	37.20	0.02	2.58
$\gamma\text{-Al}_2\text{O}_3$ powder	202.00	0.21	4.24
CX powder (before pyrolysis)	345.18	0.35	4.05
CX powder	691.41	0.44	2.55
2Co/ACX0	2.77	1.16	/
2Co/A($\gamma\text{-Al}_2\text{O}_3$)	21.05	0.05	9.29
2Co/ACX1	49.33	0.05	3.80
2Co/ACX2	44.87	0.05	4.12
2Co/ACX3	37.05	0.03	3.37
2Co/ACX4	35.52	0.03	3.35

S_{BET} : Specific surface area; V_T : Total pore volume; D_p : Average pore diameter.

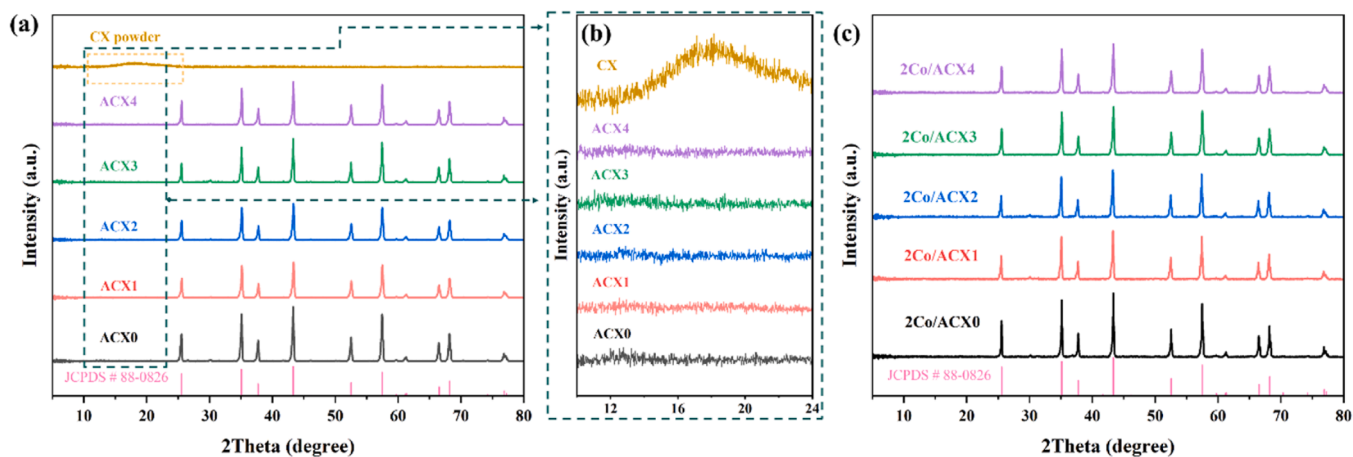


Fig. 1. XRD patterns of (a) samples before and after RF-derived CX loadings, (b) the magnified x-axis for ACXx samples, and (c) ACXx samples after cobalt incorporation.

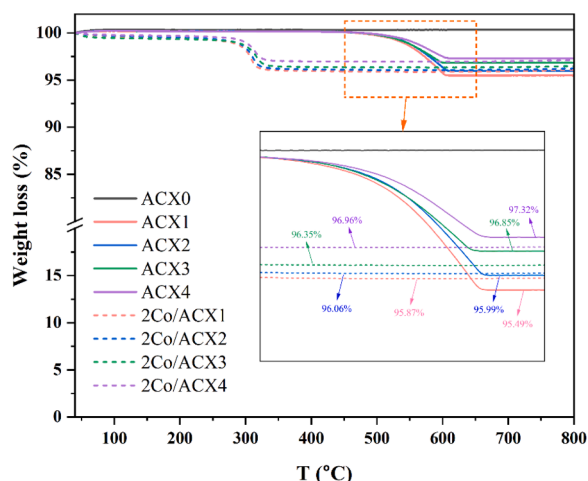


Fig. 2. TGA profiles of ACX x and 2Co/ACX x in air atmosphere with a heating rate of 5 °C/min.

the [Supplementary information \(Text S1\)](#). For comparison, the surface areas for pure γ -Al $_2$ O $_3$ and carbon xerogel powders were 202.00 m 2 /g and 691.41 m 2 /g, respectively.

Additionally, the average pore diameter of ACX0 dropped from 387.5 nm (mercury intrusion results as reported in our recently published work [9]) to 5.78 nm, 3.15 nm, 2.39 nm, 2.59 nm, and 2.58 nm after modified with γ -Al $_2$ O $_3$, ACX1, ACX2, ACX3, and ACX4, respectively. This indicates the successful incorporation of high-surface-area materials, which might contribute to more accessible active sites for the high dispersion of cobalt-based catalysts on the alumina beads, thereby higher catalytic efficiency in the chemical reaction process. Simultaneously, the nanoconfined space may enrich pollutant molecules in the pores [29]. After cobalt incorporation, all samples exhibited a similar slight decrease trend in BET surface area and increase in average pore diameter. Studies related to doping with metallic oxides reveals a similar pattern, typically attributed to the reduction in micropores that

were partially obstructed by the metallic oxide particles [30,31]. In this sense, the reduction in S_{BET} for 2Co/ACX x samples was probably associated with the introduction cobalt oxide, particularly the partial blockage of microporosity by the Co $_3$ O $_4$. That, in turn, evidences the successful incorporation of cobalt-based catalysts.

The thermal behaviour of ACX x and 2Co/ACX x samples shown in [Fig. 2](#) was examined by TGA analysis throughout the temperature range of 40–800 °C under a flow of air. This was conducted to determine the actual content of carbon xerogels, as carbon xerogels can be completely decomposed into CO $_2$ and H $_2$ O in the presence of oxygen. For ACX0 beads composed of α -Al $_2$ O $_3$, there was negligible weight loss, indicating the superior thermal stability of the base alumina beads. In contrast, samples after carbon xerogel modification experienced a weight loss when the temperature reached at approximately 600 °C. It can be seen from the inset that the residual weights of ACX1, ACX2, ACX3, and ACX4 at 800 °C were 95.49 %, 95.99 %, 96.85 %, and 97.32 %, respectively, corresponding to a total weight loss of 4.51 %, 4.01 %, 3.15 %, and 2.68 %. These results could confirm the weight percentage of carbon xerogels in each sample due to the consumption of carbon matrix in the air atmosphere. The weight loss results exhibited a downward trend as the CX sol concentration decreased, which are also in concordance with the experimental findings on carbon xerogel mass fraction during the sample preparation process, as shown in [Table S1](#). Compared to the TGA results for ACX x samples prior to cobalt loading, 2Co/ACX x samples experienced two weight loss stages, occurring between 40 and 290 °C and 290–325 °C. The initial stage, showing only a 1.1 % weight loss, could be ascribed to the minimal consumption of Co $_3$ O $_4$, as documented in the literature [32], while the subsequent stage was related to the decomposition of carbon xerogels in an air atmosphere, similar to what was observed in ACX x samples. It is important to emphasize that the transformation of Co $_3$ O $_4$ from cobalt precursor under nitrogen flow was verified by the TGA profile of cobalt nitrate hexahydrate ([Fig. S3 \(a\)](#)) and XRD pattern ([Fig. S3 \(b\)](#)). A detailed discussion was provided in the [Supplementary information \(Text S2\)](#). Likewise, a similar decline trend in carbon xerogel contents for 2Co/ACX x samples was observed, but the decomposition temperature reduced to 320 °C. This can be linked to the interactions between cobalt oxide and carbonaceous materials. Gao

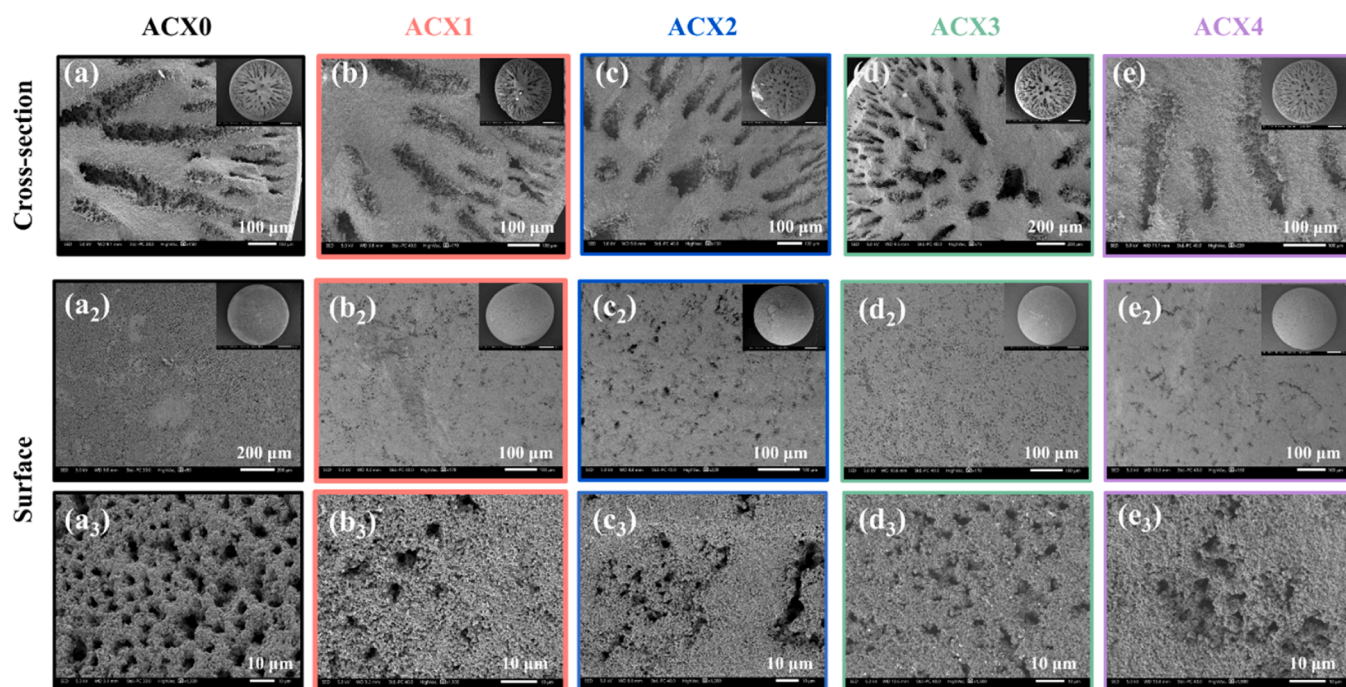


Fig. 3. SEM images of the cross-sectional views of (a) microchannel-structured alumina beads (ACX0), and CX dip-coated alumina beads: (b) ACX1, (c) ACX2, (d) ACX3, and (e) ACX4; and the surface views of (a $_2$, a $_3$) ACX0, (b $_2$, b $_3$) ACX1, (c $_2$, c $_3$) ACX2, (d $_2$, d $_3$) ACX3, and (e $_2$, e $_3$) ACX4.

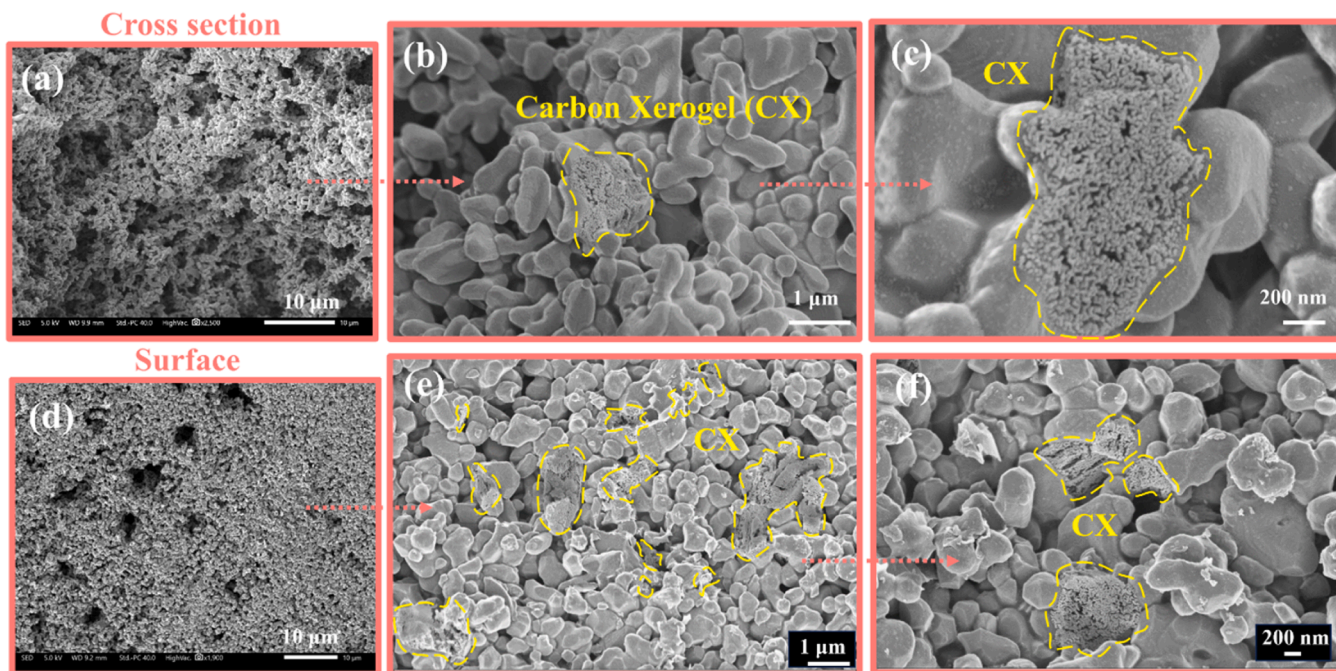


Fig. 4. High magnification SEM images of (a–c) finger-like microstructures in the cross-section and (c–e) surface of ACX1.

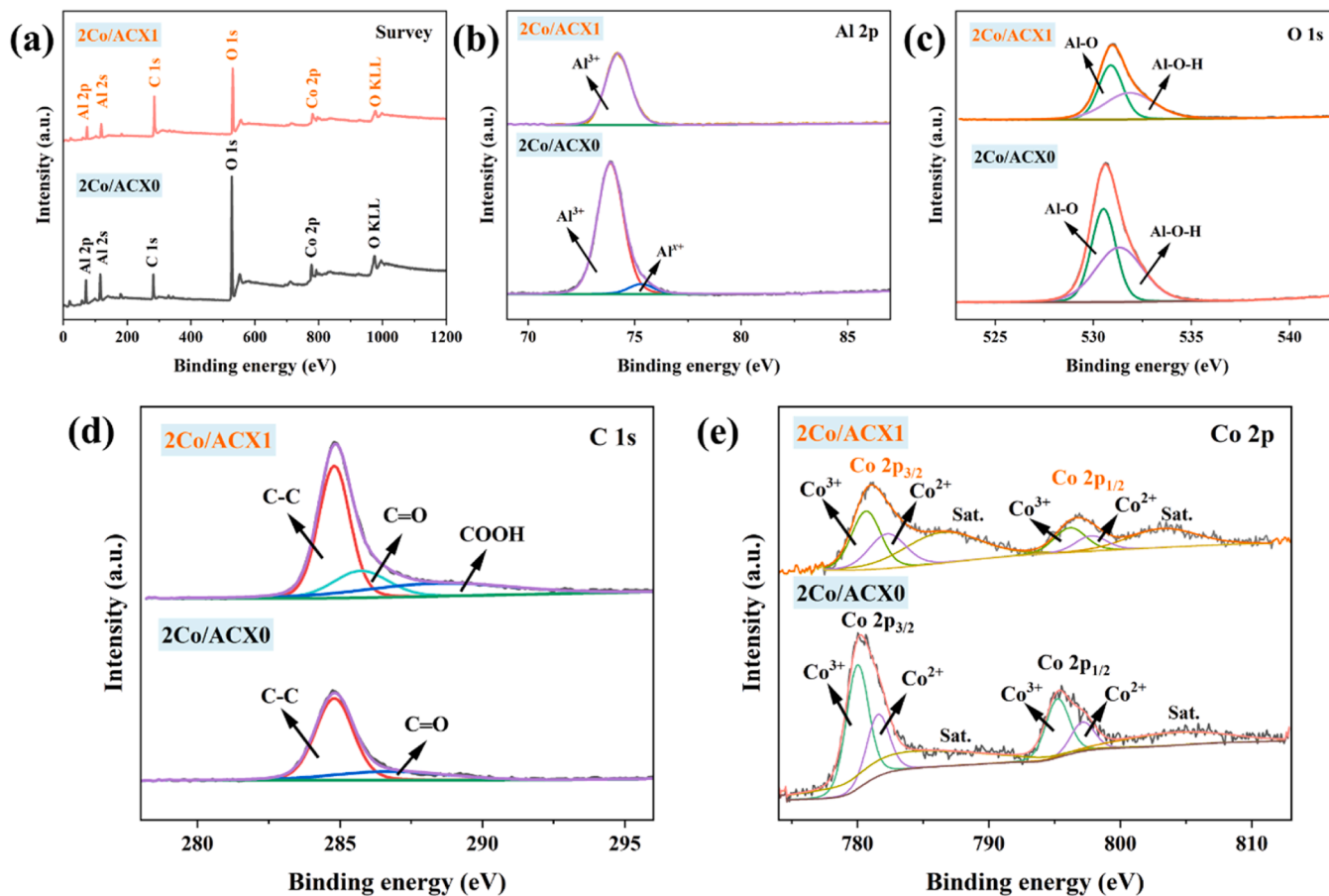


Fig. 5. (a) XPS survey spectra, and high-resolution XPS spectra of (b) Al 2p, (c) O 1s, (d) C 1s, and (e) Co 2p of cobalt-impregnated microchannel-structured alumina beads before (2Co/ACX0) and after CX loadings (2Co/ACX1).

et al. observed a similar phenomenon of which the initial decomposition temperature decreased from 522 °C to 255–270 °C as the Co_3O_4 content increased [33].

3.2. Morphological analysis

Fig. 3 depicts the SEM images of samples before (ACX0) and after carbon xerogel modifications (ACX1–4) at different magnification levels. The cross-sectional views in Fig. 3(a–e) revealed that all samples possessed radial finger-like microchannels, with no significant differences observed among them. This is due to the fact that carbon xerogels consisted of microclusters assembled by microspheres at the nanometre scale, as highlighted by the higher magnification morphologies of ACX1 shown in Fig. 4(a–c). This result aligns with the SEM images of RF-derived carbon xerogel reported in the literature [34]. Regarding the surface views, ACX0 (Fig. 3(a₂, a₃)) exhibited numerous exposed open channels, but as the sol concentrations increased, these channels were partially obstructed by carbon xerogels, particularly ACX1 with the highest concentration of carbon xerogel. Moreover, as illustrated in Fig. 4(d–f), numerous carbon xerogels were detectable on the surface of ACX1 at high magnifications, further confirming the successful incorporation of carbon xerogel washcoatings.

Fig. S4 displayed the SEM images of two representative samples, i.e., ACX1 and ACX3, after incorporating 2 wt% Co_3O_4 by a simple impregnation method. The introduction of Co_3O_4 did not alter the original morphologies, such as finger-like microchannels in the cross-section and exposed open channels on the surface, of both alumina beads. It can be seen from Fig. S4 (a₂, a₃) and Fig. S4 (b₂, b₃) that 2Co/ACX3 exhibited more noticeable exposed open channels due to the lower carbon xerogel loadings and sol concentrations, leading to the less partially blocked pores by carbon xerogels, which is in accordance with the SEM images of ACX1 (Fig. 3(b₂)) and ACX3 (Fig. 3(d₂)) before cobalt incorporation.

3.3. XPS analysis

To verify the presence of Co element and probe the chemical valence state of 2Co/ACXx samples, XPS spectra of 2Co/ACX0 and 2Co/ACX1 were analysed. As shown in Fig. 5(a), the XPS survey spectra confirmed the presence of elements Al, O, C and Co in both samples. The corresponding high resolution XPS spectra of Al 2p (Fig. 5(b)), O 1s (Fig. 5(c)), and Co 2p (Fig. 5(e)) revealed that the existence of CX sol coatings in 2Co/ACX1 resulted in lower intensities of the Al 2p, O 1s, and Co 2p spectra. Simultaneously, an extremely weak peak centred at 75.3 eV in 2Co/ACX0, which was linked to the formation of small amounts of aluminium suboxide during the cobalt impregnation process [9,35,36], disappeared in the 2Co/ACX1 sample. These findings could be attributed to the presence of carbon xerogels, which is consistent with the BET results (Table 1) [37,38]. As noted, cobalt oxide was not detected in the XRD patterns, but the Co 2p spectra revealed that cobalt was present in two chemical states (Co^{3+} , Co^{2+}) in both 2Co/ACX0 and 2Co/ACX1, corresponding to the compositions of Co_3O_4 .

In contrast, the C 1s spectra in Fig. 5(d) displayed a higher intensity for 2Co/ACX1 compared to 2Co/ACX0. This increased intensity was directly linked to the additional carbon source from the carbon xerogel in 2Co/ACX1. As observed, the deconvolution of the XPS spectra for the C 1s regions revealed two peaks for 2Co/ACX0 and three peaks for 2Co/ACX1. The adventitious carbon centred at 284.8 eV in both samples was originated from the carbon grid during sample preparation process [39]. Both peaks centred at 286.4 eV and 285.9 eV were assigned to C=O bond, as reported by Kim et al. [40]. They indicated that peaks within the 285.9–286.4 eV range are associated with C=O bond in phenol, alcohol, and ether, etc. In addition, the third peak existed in 2Co/ACX1 at 288.8 eV was attributed to carbon in carboxylic groups [15,41]. Consequently, the XPS spectra verified the presence of Co element in two chemical valence states, as well as the successful incorporation of CXs.

3.4. Evaluation of the catalytic activity

3.4.1. Effect of SMX concentrations and reaction temperature

The introduction of CXs improved the dispersion of the catalytic active phase, leading to more accessible active sites participating in the catalytic reaction, which is expected to result in enhanced catalytic activity. In this work, the catalytic performance of novel 2Co/ACXx samples was investigated by the degradation of organic pollutants in a PMS-activated AOPs reaction system. The influences of SMX concentrations (10 mg/L, 20 mg/L, and 40 mg/L), reaction temperatures (20 °C, 30 °C, and 40 °C), organic pollutant types (SMX, p-HBA, phenol, and MO), the contribution of the BET surface area, and washcoating properties ($\gamma\text{-Al}_2\text{O}_3$ sol washcoatings as reference, carbon xerogel sol washcoatings as primary) were all included, as shown in Fig. S5, Fig. 6, Fig. 7, Fig. 9, Fig. S6, and Fig. S7. For all SMX degradation reactions, the blank experiments, which involved the 2Co/ACX1 catalyst alone without the addition of PMS, demonstrated negligible catalytic performance (< 0.1 %).

Fig. 6(a) depicts the degradation of 20 mg/L SMX at 20 °C. The results demonstrated that the removal efficiency for PMS only, 2Co/ACX0, 2Co/A($\gamma\text{-Al}_2\text{O}_3$), 2Co/ACX1, and 2Co/ACX3 was 26.4 %, 34.9 %, 52.2 %, 99.2 %, and 97.0 %, respectively. Meanwhile, the reaction kinetics in Fig. 6(b) and the corresponding rate constants in Fig. 6(c) were consistent with the catalytic performance. It is obvious that 2Co/ACX1 with the highest BET surface areas possessed the highest catalytic activity, and the rate constant of 2Co/ACX1 was 15.3 times, 10.9 times, and 6.3 times higher than those of PMS alone, 2Co/ACX0, and 2Co/A($\gamma\text{-Al}_2\text{O}_3$), respectively. This was further validated during the degradation of 10 mg/L SMX, as illustrated in Fig. S5 and Text S3 in the Supplementary information. The remarkably boosted catalytic performance may be related to the enhanced S_{BET} , and this will be further explored in the subsequent reactions.

Fig. 6(b) demonstrated that this pattern persisted when the SMX concentration was raised to 40 mg/L, though the differences between 2Co/ACX1 and 2Co/ACX3 became slightly less pronounced. The diminishing difference is probably owing to more exposed open channels on the bead surfaces, as corroborated by the SEM images in Fig. S4 (a₃, b₃), which contributed to reducing the mass transfer resistance at higher pollutant concentrations. It is widely recognized that high pollutant concentrations typically increase the demand for accessible active sites, and a greater number of open channels on the surface certainly aids in transporting more pollutants into the microchannels to interact with the active sites. This aligns with our recent published work at high SMX concentrations [9]. However, this restricted mass transfer could be improved by increasing the reaction temperature to 30 °C, because the diffusion coefficient increases with rising temperature, according to Arrhenius equation [42]. As a result, the degradation efficiency of 2Co/ACX1 and 2Co/ACX3 followed the trend of 40 °C > 30 °C > 20 °C, a pattern also observed in the reaction kinetics (Fig. 6(e)) and the corresponding rate constants (Fig. 6(f)).

3.4.2. Effect of catalyst dosage and pH

Besides the effects of SMX concentrations and reaction temperatures, the degradation of SMX was also studied under varying catalyst dosages and pH levels, as depicted in Fig. 7. As expected, the SMX removal progressively increased from 21.3 % to 92.2 % within 30 min with the catalyst dosage increased from 0.002 g/L to 0.2 g/L, thanks to more accessible active sites for PMS activation. This, in turn, generated more reactive radicals, such as $\text{SO}_4^{\cdot-}$ and $\cdot\text{O}_2$, for the efficient degradation of organic pollutants. In this work, a catalyst dosage of 0.02 g/L was selected as the target for SMX elimination, except for Fig. S6, where 0.2 g/L of catalyst was used in all reactions to assess the catalytic activity at higher catalyst dosages.

Fig. 7(b) shows the SMX removal efficiency at an initial pH range of 3–11. At pH levels of 5–10, the degradation efficiency remained robust, consistently nearly 100 %. However, the degradation rate decreased

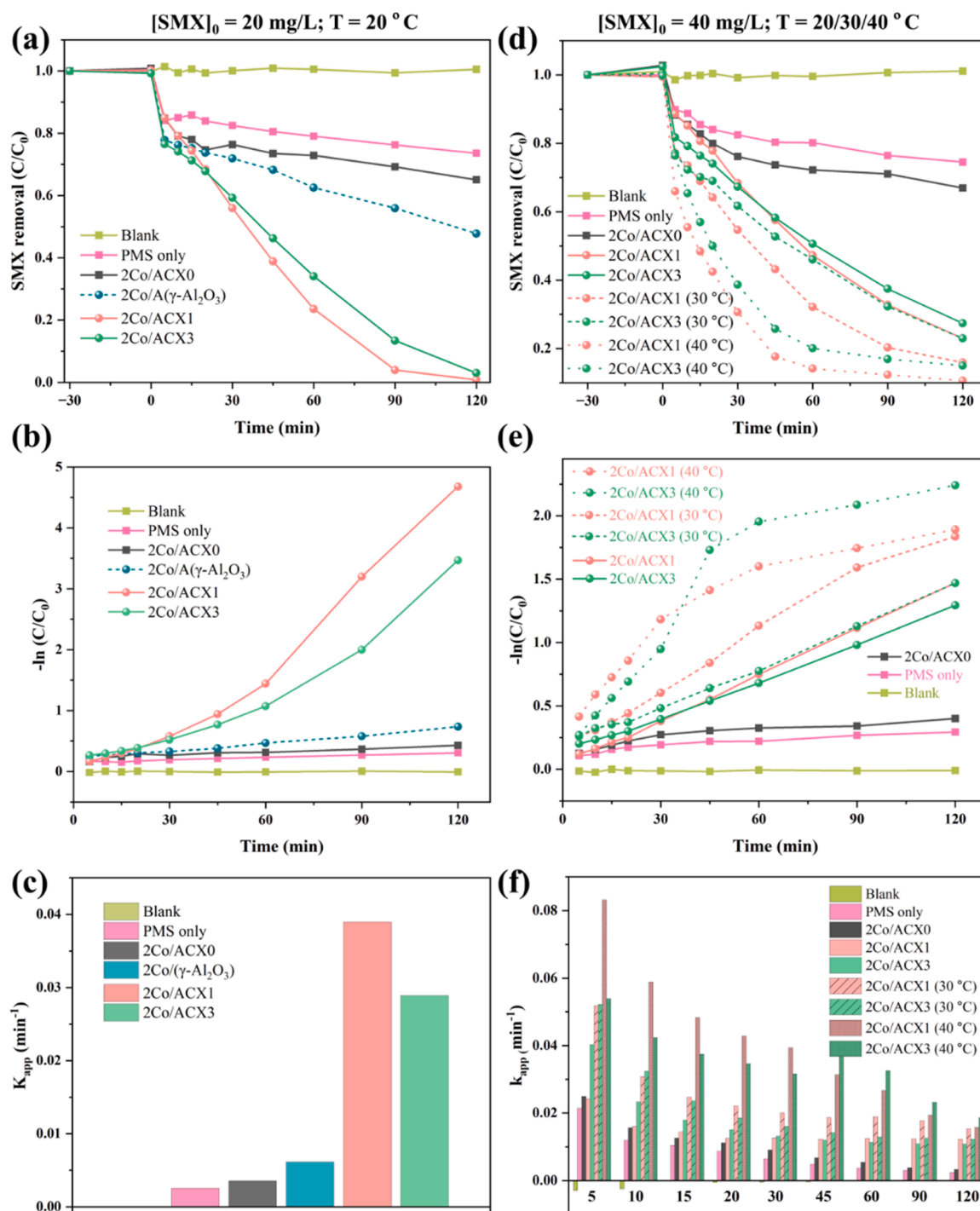


Fig. 6. (a) Degradation of 20 mg/L SMX using three types of catalysts at 20 °C, (b) their reaction kinetics, and (c) the corresponding rate constants; (d) Degradation of 40 mg/L SMX using three types of catalysts at three reaction temperatures, (e) their reaction kinetics, and (f) the corresponding rate constants during the whole reaction process. Reaction Conditions: [PMS]₀ = 0.31 mM, [catalyst]₀ = 0.02 g/L, $r = 150$ rpm.

under strong acid and base conditions, with 86.9 % of SMX breaking down at pH 3 and only 16.2 % at pH 11, even though the efficiency remained satisfactory at pH 3. This is due to the fact that, on the one hand, in strong acid solutions, excess H⁺ consumes HSO₅⁻, preventing the redox cycle of Co (II)/Co (III), and consequently poor SMX degradation [43]; On the other hand, in strong base solutions, the main reactive species, SO₄⁻ (E° = 2.5–3.1 V, t_{1/2} = 30 μs), transformed to ·OH with lower redox potential (E° = 1.8–2.7 V) and a shorter half-life time (t_{1/2} = 20 ns) [44,45].

3.4.3. Preliminary analysis of PMS activation by carbon xerogels

Carbon materials containing oxygen-functional groups, such as -COOH and C=O, have been reported to activate PMS [46], thereby facilitating the catalytic activity. To the best of our knowledge, reported work on carbon xerogels for AOPs are scarce, including Co and Fe in carbon xerogels [47] and N-doped carbon xerogels [48]. However, in order to explore the role of carbon xerogels in PMS activation, we conducted a preliminary analysis of catalytic reactions using a spectrophotometer (UV-Vis Evolution 220, Thermo Scientific), as illustrated in Fig. 8 and Fig. S8. Fig. 8 displays the UV-Vis spectra of SMX

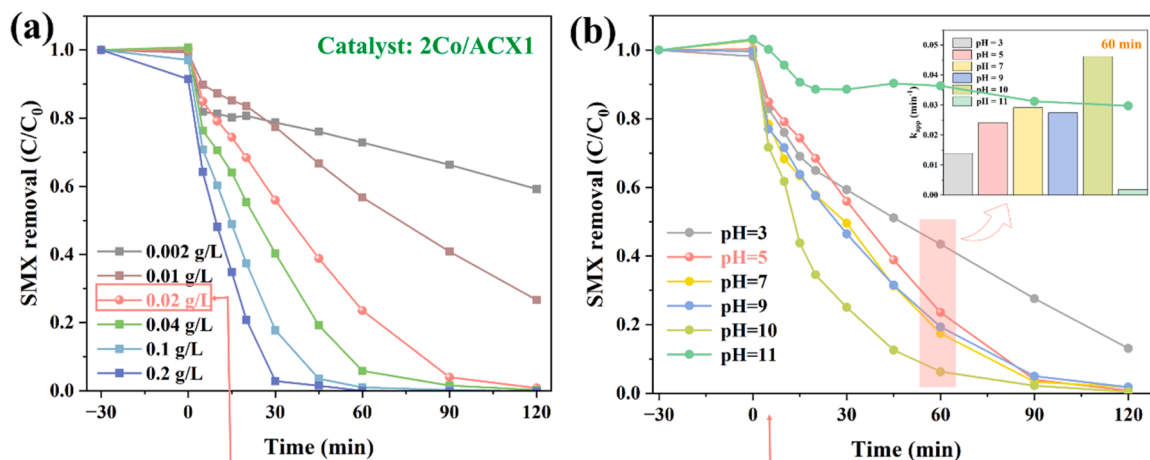


Fig. 7. (a) Effect of catalyst dosage and (b) initial solution pH on the degradation of 20 mg/L SMX using 2Co/ACX1. Reaction Conditions: $[PMS]_0 = 0.31$ mM, $T = 20$ °C, $r = 150$ rpm.

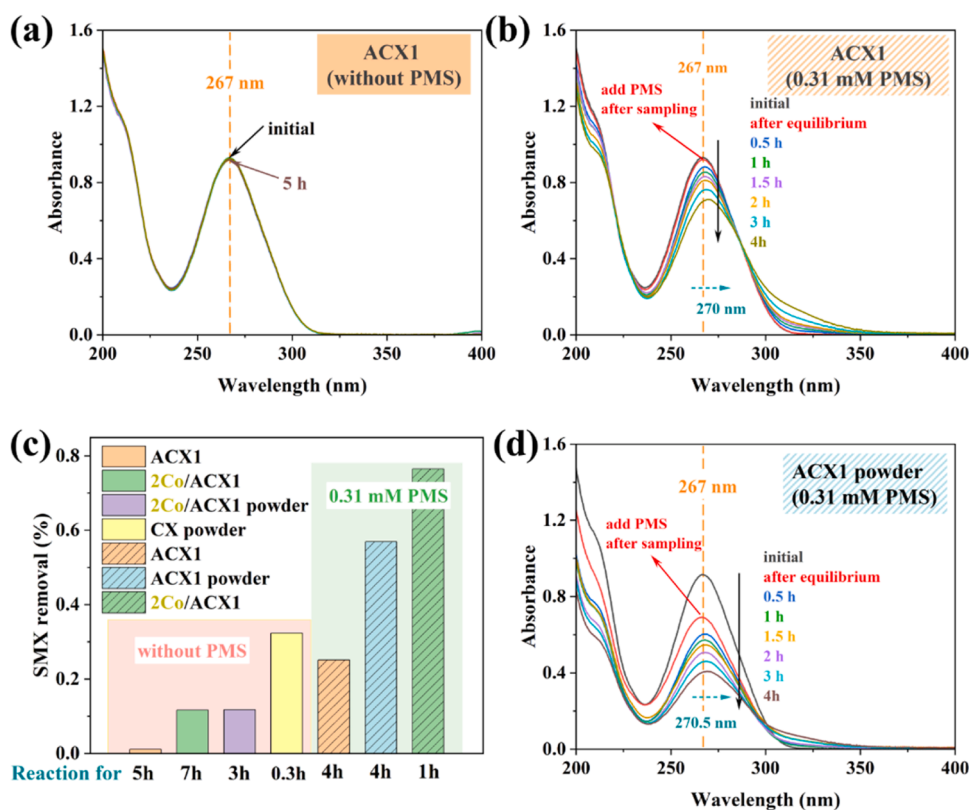


Fig. 8. UV-Vis spectra of (a) ACX1 without PMS, (b) ACX1 with 0.31 mM PMS, and (d) ACX1 powder with 0.31 mM PMS for the degradation of SMX; (c) SMX degradation with different catalysts in the presence and absence of PMS. Reaction conditions: $[SMX] = 20$ mg/L, $[catalyst]_0 = 0.2$ g/L, $T = 20$ °C, $r = 150$ rpm.

concentrations over time during reactions with different catalysts. The results indicated that ACX1, i.e., 2Co/ACX1 before cobalt loading, showed minimal degradation of SMX in the absence of PMS (Fig. 8(a)). However, when PMS was added, ACX1 could degrade 25.1 % of SMX within 4 h (Fig. 8(b)), accompanied by a wavelength shift from 267 nm to 270 nm. This red shift in the absorption edge is consistent with the 2Co/ACX1 result in Fig. S8 (c), implies that PMS was activated by ACX1 even without a cobalt catalyst [49]. Additionally, ACX1 powder (obtained by grinding ACX1) exhibited enhanced SMX degradation (56.9 % in 4 h) and a more pronounced red shift in absorption (Fig. 8(d)). On the one hand, this highlighted the significance of mass transfer in catalytic reactions, as catalyst powder typically diffuses faster than large beads;

on the other hand, we can conclude that PMS could be activated by carbon xerogel-based materials. For comparison, Fig. S8 (a, b, d) shows the absorption spectra of 2Co/ACX1, 2Co/ACX1 powder, and CX powder in the absence of PMS, where SMX degradation occurred without a shift in the absorption edge. This indicates that this degradation process was attributed to the adsorption capacity of the carbon xerogel, as supported by Fig. S9.

3.4.4. Effect of organic pollutants

For practical applications, the catalytic ability of materials for different types of organic pollutants is pivotal. To further study the capability of the 2Co/ACX1/PMS system, degradation of phenols (p-HBA

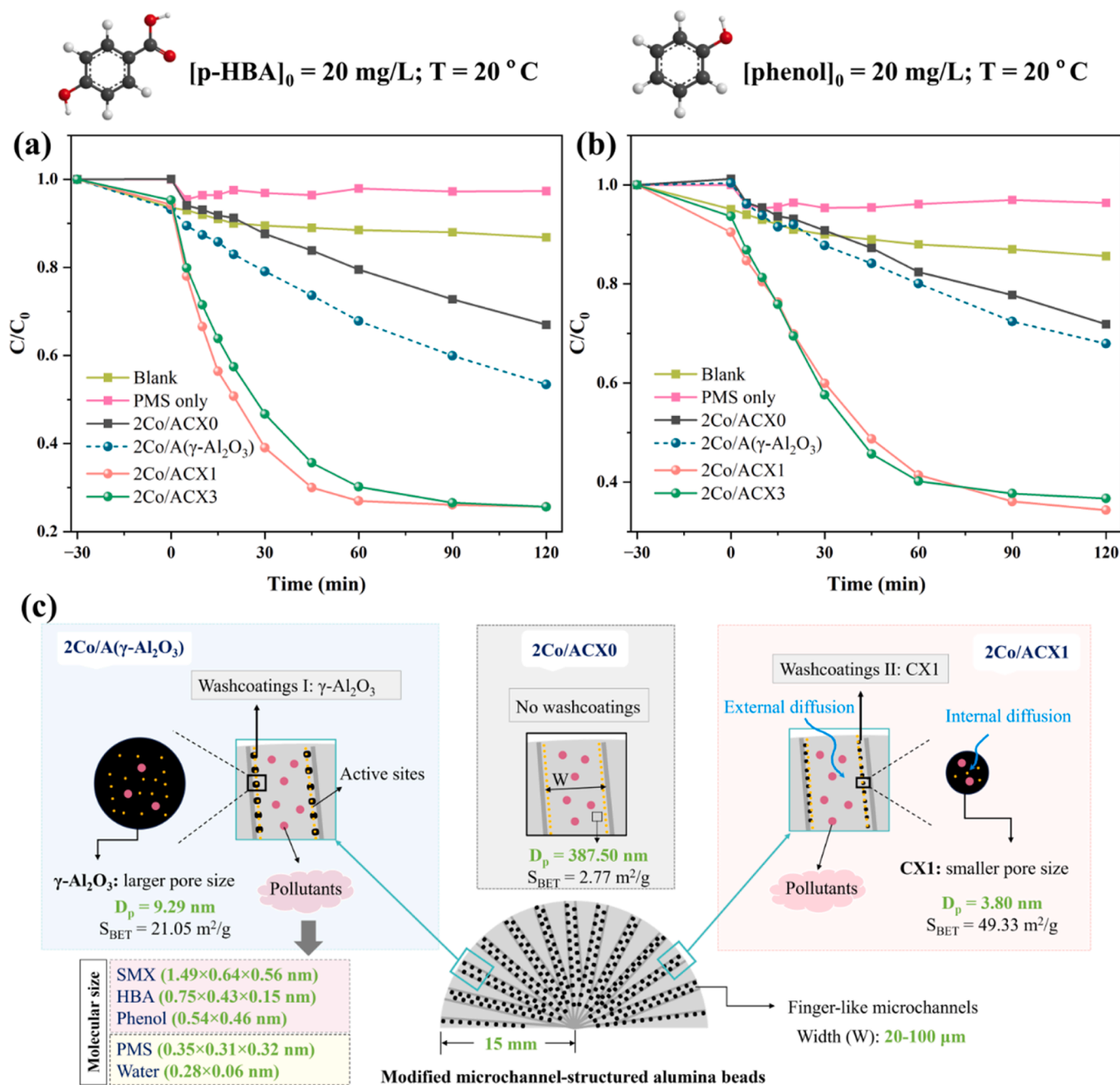


Fig. 9. Degradation of (a) 20 mg/L p-HBA and (b) 20 mg/L phenol using three types of catalysts; (c) A schematic diagram illustrating three types of catalysts with (2Co/A(γ -Al₂O₃) and 2Co/ACXx) and without (2Co/ACX0) washcoatings. Reaction Conditions: [PMS]₀ = 0.31 mM, [catalyst]₀ = 0.1 g/L, T = 20 °C, r = 150 rpm.

and phenol) and dyes (MO) was assessed, as shown in Fig. 9 and Fig. S7. Fig. 9 provided compelling evidence for the efficacy of p-HBA and phenol elimination using the 2Co/ACXx samples, drastically surpassing the performance of 2Co/ACX0 and 2Co/A(γ -Al₂O₃), aligning with the SMX removal in Fig. 6 and Figs. S5–6. In the case of blank experiments for the degradation of these two pollutants, 2Co/ACX1 sample alone oxidized 13.2 % of p-HBA and 14.4 % of phenol without the addition of PMS. This can be ascribed to the adsorption capacity of carbon xerogels. Comparable results for p-HBA and phenol adsorption on various carbon materials have been documented in the literature [24,50,51]. It is crucial to point out that the considerably high adsorption capacity of CX powder, beyond that of γ -Al₂O₃ – both the commercial ones and the sol-gel type used in this study – has been proven in Fig. S9. Furthermore, a similarly substantial enhancement in MO elimination using 2Co/ACX1 is also discovered in Fig. S7.

Based on the above catalytic results, the exceptional catalytic performance of 2Co/ACXx samples in all reactions has been validated. This can be attributed to a synergistic effect of the following factors: (a) The enhanced BET surface area of 2Co/ACX1 unquestionably contributed to improving the dispersion of the catalytic active phase, i.e., cobalt oxide, thereby facilitating the generation of more reactive radicals for the reaction; (b) In comparison to both the base alumina beads (2Co/ACX0) and γ -Al₂O₃-modified alumina beads (2Co/A(γ -Al₂O₃)), carbon xerogel in CX-modified alumina beads (2Co/ACXx) also contributed to the catalytic reaction by boosting the adsorption capacity for the degradation of organic pollutants; (c) The doped carbonaceous materials could catalyse the self-decomposition of PMS to generate reactive oxygen species [13,52–54], so partial PMS activation by carbon xerogels might be advantageous in the 2Co/ACXx/PMS as well; (d) The nanoconfined pore effect on PMS activation within the nanoparticles of 2Co/ACXx samples

($D_p = 3.80\text{--}4.12\text{ nm}$) could play a role in accelerating chemical reactions, as interactions between the nanoconfinement and either reactants (organic pollutants including SMX, p-HBA, phenol, and MO), oxidizing agent (PMS), the transition state, the product, or the catalysts (2Co/ACXx) in a nanoconfined space may alter the reaction energy diagram [29,55].

As exemplified in Fig. 9(c), the bare microchannel-structured alumina beads have catalysts directly loaded onto the substrates with a large pore size of 387.50 nm, based on the mercury intrusion data from our recently published paper [9]. After applying a washcoat of $\gamma\text{-Al}_2\text{O}_3$ or carbon xerogels, however, the catalysts could be deposited on the washcoating layers, where the pore diameters were lowered to 9.29 nm for $\gamma\text{-Al}_2\text{O}_3$ and 3.80 nm for CX. Taking into account the molecular sizes of PMS ($0.315 \times 0.305 \times 0.350\text{ nm}$), SMX ($1.49 \times 0.64 \times 0.56\text{ nm}$), p-HBA ($0.75 \times 0.43 \times 0.15\text{ nm}$), phenol ($0.54 \times 0.46\text{ nm}$), and water molecules ($0.28 \times 0.06\text{ nm}$) [56–59], the smaller pore diameter in 2Co/ACXx samples could allow up to twelve layers of PMS molecules to diffuse into the nanopores and interact with the catalytic active phase, resulting in a confinement effect that improved the utilisation of short-lived reactive oxygen species; (e) The tremendous diffusional mass transfer in the three-millimetre diameter alumina beads with finger-like microstructures promoted the transport of reactants and products, which, in turn, improved the catalytic reactions across all three types of alumina beads. In short, the synergistic process intensification at the microscale process unit, i.e., microchannel-structured alumina beads paired with functional carbon xerogels, ended the system with the exceptional catalytic performance for the decontamination of various

organic pollutants.

3.4.5. Possible catalytic reaction pathways and mechanism

A series of selective radical quenching agents (10 mM NaN_3 , 10 mM p-BQ, 1 M MeOH, 1 M tBA) were introduced to the 2Co/ACX1|PMS reaction system to assess the contribution of each reactive species, as shown in Fig. 10 (a). When NaN_3 and p-BQ were added, the SMX removal efficiency was suppressed from 99.19% to 7.30% and 54.82%, respectively. This might be related to the crucial roles of $^1\text{O}_2$ [9] and $\cdot\text{O}_2^-$ [27]. However, it has been recently reported that NaN_3 and p-BQ may also quench $\text{SO}_4^{\cdot-}$ and $\cdot\text{OH}$ [60–62], so additional evidence – electron paramagnetic resonance (EPR) – were conducted to further verify their contributions in AOPs. As illustrated in Fig. 10 (c), when 2,2,6,6-tetramethyl-4-piperidone (TEMP) was added into 2Co/ACX1|PMS reaction system, distinct three-line signals with peak strength of 1:1:1 for TEMP- $^1\text{O}_2$ were detected, and the intensity increased as the reaction time progressed from 10 min to 20 min. In contrast, the addition of 5,5-dimethyl-1-pyrroline N-oxide (DMPO) (Fig. 10 (d)) resulted in the formation of $\cdot\text{O}_2^-$ signals. This served as direct evidence for the formation of $^1\text{O}_2$ and $\cdot\text{O}_2^-$ [27,63].

Additionally, tBA performed a minimal inhibitory effect, less than 4.7%, on SMX removal in the range of 100 mM to 1000 mM (Fig. S10 (a)), revealing the negligible contribution of $\cdot\text{OH}$ [64], although distinct four-line signals with peak strength of 1:2:2:1 for DMPO- $\cdot\text{OH}$ were detected in Fig. 10 (e) [61]. Furthermore, as MeOH can react with both $\cdot\text{OH}$ ($k = 9.7 \times 10^8\text{ M s}^{-1}$) and $\text{SO}_4^{\cdot-}$ ($k = 2.5 \times 10^7\text{ M s}^{-1}$) [59], the massive suppression of SMX removal by MeOH suggested that $\text{SO}_4^{\cdot-}$ was

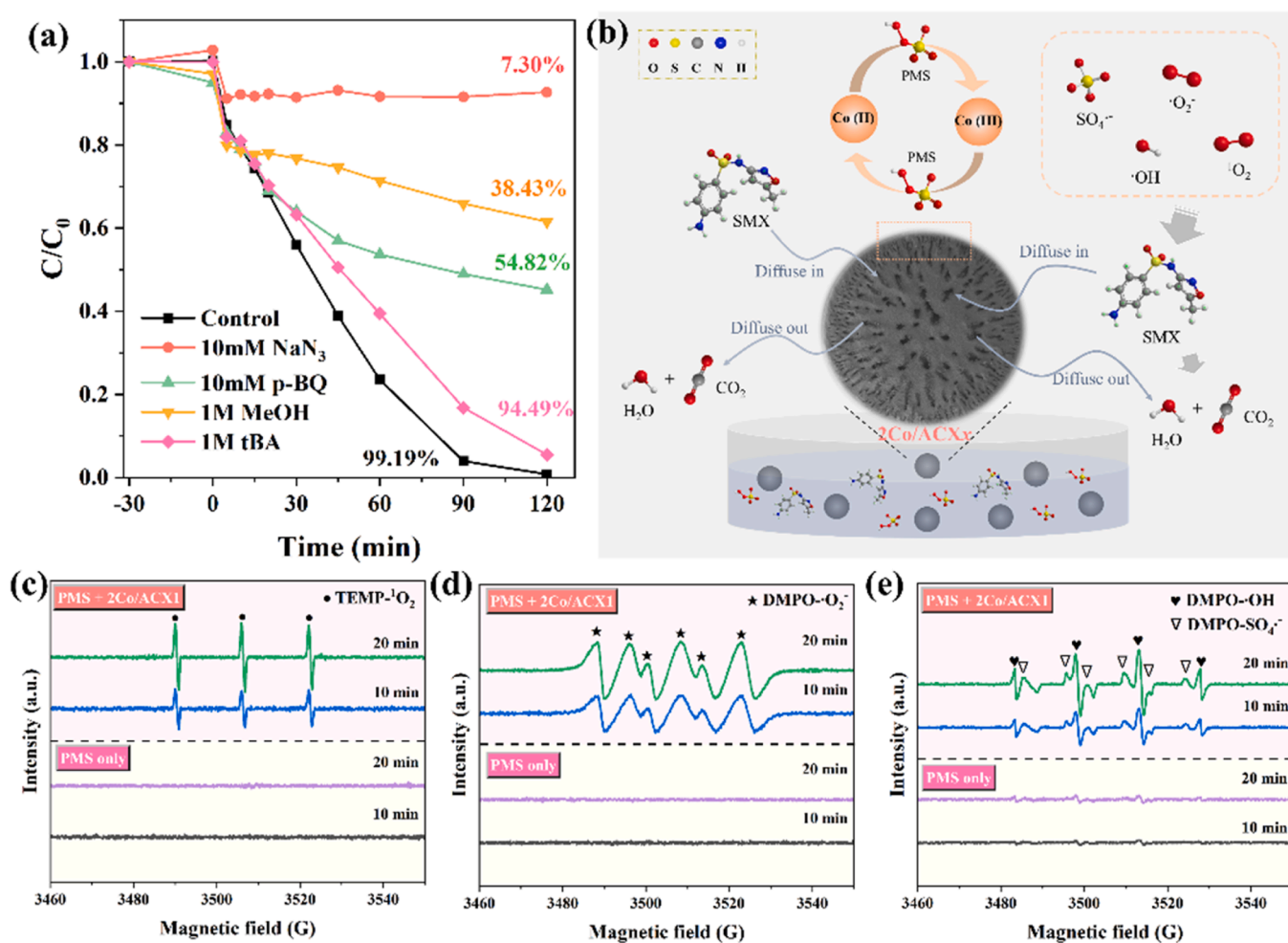


Fig. 10. (a) Effect of quenching agents on degrading SMX (catalyst: 2Co/ACX1); (b) A proposed mechanism for catalytic oxidation of SMX by 2Co/ACX1; EPR signals detected in 2Co/ACX1|PMS system for (c) TEMP- $^1\text{O}_2$ adducts, (d) DMPO- $\cdot\text{O}_2^-$, and (e) both DMPO- $\cdot\text{OH}$ and DMPO- $\text{SO}_4^{\cdot-}$.

the primary ROS in the system. Similarly, 1000 mM MeOH efficiently quenched $\cdot\text{OH}$ and $\text{SO}_4^{\cdot-}$, as evidenced by Fig. S10 (a), where various amounts of MeOH were added and stabilised at 1000 mM. The generation of $\text{SO}_4^{\cdot-}$ can be evidenced by the detection of six-line signals corresponding to DMPO- $\text{SO}_4^{\cdot-}$ adducts in Fig. 10 (e) [63]. It is also important to note that the weak signals for DMPO- $\cdot\text{OH}$ and DMPO- $\text{SO}_4^{\cdot-}$ observed with PMS alone in Fig. 10 (e) align with the self-degradation of contaminants when catalysts were absent in Fig. 6, Fig. S5, Fig. S6, Fig. 9, and Fig. S7.

Moreover, the reaction rate constants (k) are consistent with the quenching experiment, as shown in Fig. S10 (b). It is also worth noting that the quenching experiments across the three systems (Fig. S11 (a)) revealed only slight variation in the contributions of active species, with a ranking order of $\text{SO}_4^{\cdot-} > \cdot\text{O}_2 > \cdot\text{OH}$ and a difference range of 6–11 %. Notwithstanding the deficiency of definitive evidence for the involvement of $^1\text{O}_2$ and $\cdot\text{O}_2$ for all systems, observations from the quenching results revealed a gradual increase in the role of $^1\text{O}_2$. This trend might be attributed to more frequent redox cycles driven by more accessible active sites, as $^1\text{O}_2$ can be obtained by the transformation of $\cdot\text{O}_2$, the decomposition of PMS, and the reactions of $\text{SO}_5^{\cdot-}$ (Fig. S11 (b)) [65].

Based on the quenching experiments, a possible catalytic mechanism for the degradation of SMX by 2Co/ACX1 was proposed and illustrated in Fig. 10 (b). When PMS was added to the reaction system, it quickly diffused into the finger-like microchannels (20–100 μm in width) of the ceramic beads (3 mm in diameter). Subsequently, up to twelve layers of PMS molecules ($0.315 \times 0.305 \times 0.350$ nm) further diffused into the pores of carbon xerogel washcoating layers ($D_p = 3.8$ nm), and then interacted with catalytic cobalt active phase (Co^{2+}) to trigger the reaction, generating large amounts of $\text{SO}_4^{\cdot-}$ and Co^{3+} . Meanwhile, HSO_5^- was then oxidised by Co^{3+} to yield $\text{SO}_5^{\cdot-}$, with Co^{3+} being reduced back to Co^{2+} . Therefore, the redox cycle of $\text{Co}^{2+}/\text{Co}^{3+}$ was established, facilitating the robust and long-term catalytic degradation of contaminants. As the reaction progressed, $\text{SO}_4^{\cdot-}$ radicals were partially converted into $\cdot\text{OH}$ radicals, which had a minimal role in this system but contributed to the formation of the predominant $\cdot\text{O}_2$ radicals. As noted, $^1\text{O}_2$ was produced by the conversion of $\text{O}_2^{\cdot-}$, the reactions of $\text{SO}_5^{\cdot-}$ with water or PMS, and the self-dissociation of the generated $\text{SO}_5^{\cdot-}$ (Fig. S11 (b)). In the end, the generated radicals ($\text{SO}_4^{\cdot-}$ and $\cdot\text{O}_2$) and non-radical species ($^1\text{O}_2$) reacted with the target contaminants, driving the decontamination process.

3.4.6. Reusability and stability

Cycling experiments were carried out using 2Co/ACX1 to decompose

SMX over five consecutive runs, in order to evaluate its reusability and stability for practical applications. As shown in Fig. 11 (a), the catalytic performance remained highly efficient after five recycle runs, implying the superior stability and reusability of 2Co/ACX1 catalyst. In addition, unlike powdered catalysts, these bead samples can easily separate from the bulk solution. Separation can be achieved with minimum effort through simply pouring out the aqueous solution and rinsing with deionised water. Chemical separation is estimated to account for about 10–15 % of global total energy consumption [66]. This work, however, eliminated the requirement of thermal-energy-intensive separation procedure, bringing down operational cost while preserving marvellous catalytic efficiency. Furthermore, the XRD patterns of the fresh and used samples shown in Fig. 11 (b) highlighted their extraordinary stability. It is noteworthy that the metal ions leaching for 2Co/ACX0, 2Co/ $\gamma\text{-Al}_2\text{O}_3$, and 2Co/ACX1 samples during the reusability tests have been investigated, as shown in Supplementary information (Text S4 and Fig. S12). In addition, the XPS analysis of 2Co/ACX1 after the 5th cycle (Fig. S13) further confirmed its stability, as no significant changes were observed in the valence states of the elements. Only a slight reduction in the intensity of Co 2p (Fig. S13 (b)) and C 1s (Fig. S13 (c)) was detected, potentially due to the consumption of the Co_3O_4 catalyst and minor leaching of metal ions, as evidenced by Fig. S12.

4. Conclusion

Overall, innovative modified microchannel-structured alumina beads with two types of washcoatings ($\gamma\text{-Al}_2\text{O}_3$ and carbon xerogels) have been successfully prepared by the phase-inversion and sol-gel methods. PMS-activated AOPs reaction system was selected as the catalytic system for the study. Experimental results demonstrated that the alumina beads with increased S_{BET} by incorporating CX washcoatings (2Co/ACX1) exhibited the highest catalytic activity than the base one (2Co/ACX0) and $\gamma\text{-Al}_2\text{O}_3$ washcoatings (2Co/A($\gamma\text{-Al}_2\text{O}_3$)). Under identical reaction conditions, the reaction rate of 2Co/ACX1 is 10.83 times higher than that of 2Co/ACX0 and 6.39 times higher than that of 2Co/A($\gamma\text{-Al}_2\text{O}_3$). This could be attributed to a synergistic effect resulting from a better dispersion of cobalt catalytic phase, remarkable adsorption capacity of carbon xerogels, the coexistence of two PMS activation species, nanoconfined pore effect, and reduced mass transfer resistance, within the AOPs system. The synergistic process intensification at the micro-scale process unit in this research demonstrated exceptional catalytic activity, reusability, and stability. It also effectively balanced mass transfer resistance and pressure drop, potentially fully harnessing the

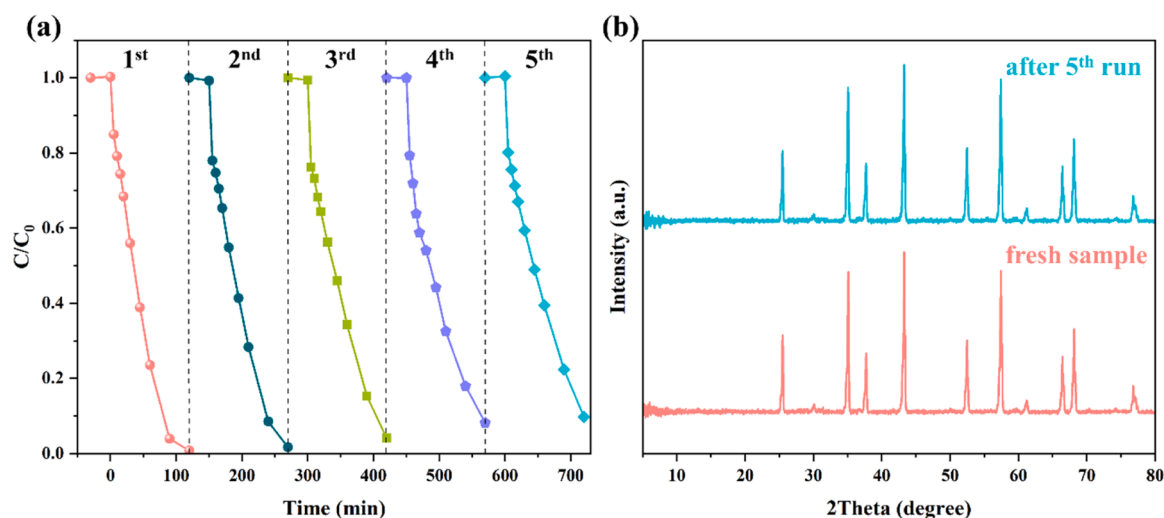


Fig. 11. (a) Recycling test of the sample 2Co/ACX1 for SMX degradation, and (b) the XRD patterns of the 2Co/ACX1 before and after 5th run. Reaction Conditions: $[\text{PMS}]_0 = 0.31$ mM, $[\text{SMX}]_0 = 20$ mg/L, $T = 20$ $^{\circ}\text{C}$, $[\text{catalyst}]_0 = 0.02$ g/L, $r = 150$ rpm.

profits of integrating nanoporous carbon materials with microchannel-structured ceramic beads for large-scale diffusion-limited chemical reactions.

Declaration of Competing Interest

The authors declare the following financial interests/personal relationships which may be considered as potential competing interests: Zhentao Wu reports financial support was provided by European Commission. If there are other authors, they declare that they have no known competing financial interests or personal relationships that could have appeared to influence the work reported in this paper.

Acknowledgements

The authors would like to acknowledge the funding support provided by the European Union's Horizon 2020 Research and Innovation Program under Grant agreement nos. 862330 (INNOMEM) and 871998 (STEPforGGR).

Appendix A. Supporting information

Supplementary data associated with this article can be found in the online version at [doi:10.1016/j.apcatb.2025.125069](https://doi.org/10.1016/j.apcatb.2025.125069).

Data availability

Data will be made available on request.

References

- Lin, Z., Zhang, Y., Min, Microfluidic plasma: novel process intensification strategy, *Green Process. Synth.* 11 (1) (2022) 1064–1071.
- Grützner, D., Ziegenbalg, R., Güttel, Process intensification – an unbroken trend in chemical engineering, *Chem. Ing. Tech.* 90 (11) (2018) 1823–1831.
- Chen, J., Deng, G., Luo, Process intensification of chemical phosphorus removal in a microreaction system, *Sep. Purif. Technol.* 330 (2024) 125544.
- Yue, J., Green process intensification using microreactor technology for the synthesis of biobased chemicals and fuels, *Chem. Eng. Process. - Process Intensif.* 177 (2022) 109002.
- Zhang, et al., ZSM-5@ceramic foam composite catalyst derived from spent bleaching clay for continuous pyrolysis of waste oil to produce monocyclic aromatic hydrocarbons, *Sci. Total Environ.* 926 (2024) 171887.
- Parsa, et al., Regenerable carbon honeycomb monoliths directly prepared from brown coal: a novel carbon product, *Chem. Eng. J.* 471 (2023).
- Vega, et al., 3D honeycomb monoliths with interconnected channels for the sustainable production of dihydroxybenzenes: towards the intensification of selective oxidation processes, *Chem. Eng. Process. - Process Intensif.* 165 (2021).
- F.C. Patcas, G.I. Garrido, B. Kraushaar-Czarnetzki, CO oxidation over structured carriers: a comparison of ceramic foams, honeycombs and beads, *Chem. Eng. Sci.* 62 (15) (2007) 3984–3990.
- Zheng, et al., Catalytic micro-structured ceramic beads and efficacy evaluation through SMX degradation in PMS-activated systems, *Sep. Purif. Technol.* 354 (2025).
- Mandić, et al., Effects of catalyst activity, particle size and shape, and process conditions on catalyst effectiveness and methane selectivity for Fischer–Tropsch reaction: a modeling study, *Ind. Eng. Chem. Res.* 56 (10) (2017) 2733–2745.
- Mazzone, et al., A compact non-PGM catalytic hollow fibre converter for on-board hydrogen production, *Sustain. Energy Fuels* 6 (6) (2022) 1554–1567.
- Hao, et al., Applications of carbon-based materials in activated peroxymonosulfate for the degradation of organic pollutants: a review, *Chem. Rec.* 23 (12) (2023) e202300203.
- Chen, et al., Decolorization of azo dye by peroxymonosulfate activated by carbon nanotube: radical versus non-radical mechanism, *J. Hazard. Mater.* 320 (2016) 571–580.
- L.T. Perez-Poyatos, et al., The dynamic ethylene adsorption on carbon xerogels as a three-way game between porosity, surface chemistry and humidity, *J. Colloid Interface Sci.* 678 (Pt A) (2024) 480–493.
- Mazzone, et al., Ruthenium-based catalysts supported on carbon xerogels for hydrogen production via ammonia decomposition, *Appl. Catal. A: Gen.* 632 (2022).
- Xiang, et al., Rapid and efficient removal of organophosphorus pollutant and recovery of valuable elements: a boosted strategy for eliminating organophosphorus from wastewater, *Water Res.* 267 (2024) 122494.
- Zhou, et al., Synthesis of carbon xerogels at varying sol-gel pHs, dye adsorption and chemical regeneration, *Chem. Eng. J.* 171 (3) (2011) 1399–1405.
- Wan, Y., Hu, W., Zhou, Catalytic mechanism of nitrogen-doped biochar under different pyrolysis temperatures: the crucial roles of nitrogen incorporation and carbon configuration, *Sci. Total Environ.* 816 (2022) 151502.
- Ye, et al., Nitrogen-doped biochar fiber with graphitization from *Boehmeria nivea* for promoted peroxymonosulfate activation and non-radical degradation pathways with enhancing electron transfer, *Appl. Catal. B: Environ.* 269 (2020).
- Zhang, et al., Non-doping 3D porous carbon with rich intrinsic defects for efficient nonradical activation of peroxymonosulfate toward the degradation of organic pollutants, *Sep. Purif. Technol.* 292 (2022).
- Stankiewicz, A.I., Process intensification: transforming chemical engineering, *Chem. Eng. Prog.* 96 (2000) 22–34.
- Tian, et al., An overview of process systems engineering approaches for process intensification: state of the art, *Chem. Eng. Process. - Process Intensif.* 133 (2018) 160–210.
- Ruhi, et al., Effect of sintering temperatures on corrosion and wear properties of sol-gel alumina coatings on surface pre-treated mild steel, *Corros. Sci.* 50 (3) (2008) 639–649.
- Wu, et al., Metal-free activation of peroxymonosulfate by boron and nitrogen co-doped graphene nanotubes for catalytic oxidation of 4-hydroxybenzoic acid, *Environ. Funct. Mater.* 1 (2) (2022) 139–148.
- Duan, et al., Insights into perovskite-catalyzed peroxymonosulfate activation: maneuverable cobalt sites for promoted evolution of sulfate radicals, *Appl. Catal. B: Environ.* 220 (2018) 626–634.
- Asif, et al., MIL-53(Fe) derived magnetic CuFe₂O₄/Fe₂O₃ composite for catalytic oxidation of sulfamethoxazole via peroxymonosulfate activation, *Chem. Eng. J.* 469 (2023).
- Zheng, et al., A visible-light-driven heterojunctioned composite WO₃/Bi(12)O(17)Cl(2): synthesis, characterization, and improved photocatalytic performance, *J. Colloid Interface Sci.* 510 (2018) 20–31.
- N.K.N. Quach, et al., Investigation of the characteristic properties of glacial acetic acid-catalyzed carbon xerogels and their electrochemical performance for use as electrode materials in electrical double-layer capacitors, *Adv. Mater. Sci. Eng.* 2017 (2017) 1–9.
- Qian, X., Gao, B., Pan, Nanoconfinement-mediated water treatment: from fundamental to application, *Environ. Sci. Technol.* 54 (14) (2020) 8509–8526.
- Bailón-García, et al., New carbon xerogel-TiO₂ composites with high performance as visible-light photocatalysts for dye mineralization, *Appl. Catal. B: Environ.* 201 (2017) 29–40.
- Kiciński, et al., Porous graphitic materials obtained from carbonization of organic xerogels doped with transition metal salts, *Bull. Mater. Sci.* 37 (1) (2014) 141–150.
- Li, et al., Facile synthesis of recyclable Co₃O₄/Co(OH)₂/RGO ternary heterostructures with synergistic effect for photocatalysis, *J. Nanopart. Res.* 20 (10) (2018).
- Gao, et al., Effect of metals and Co₃O₄ on the thermal decomposition reaction of sodium chlorate in an area of refuge, *Chem. Pap.* 74 (10) (2020) 3475–3480.
- Awadallah-F, S.A. Al-Muhtaseb, H.-K. Jeong, Selective adsorption of carbon dioxide, methane and nitrogen using resorcinol-formaldehyde-xerogel activated carbon, *Adsorption* 23 (7–8) (2017) 933–944.
- Song, et al., Fabrication of super slippery sheet-layered and porous anodic aluminum oxide surfaces and its anticorrosion property, *Appl. Surf. Sci.* 355 (2015) 495–501.
- Tago, et al., XPS study from a clean surface of Al₂O₃ single crystals, *Procedia Eng.* 216 (2017) 175–181.
- Zou, et al., Electrochemical oxidation and advanced oxidation processes using a 3D hexagonal Co₃O₄ array anode for 4-nitrophenol decomposition coupled with simultaneous CO₂ conversion to liquid fuels via a flower-like CuO cathode, *Water Res.* 150 (2019) 330–339.
- Guo, et al., Co₃O₄ modified polymeric carbon nitride for external light-free chlorine activating degradation of organic pollutants, *J. Hazard. Mater.* 429 (2022) 128193.
- Zheng, et al., A visible-light-driven heterojunctioned composite WO₃/Bi₂O₇Cl₂: synthesis, characterization, and improved photocatalytic performance, *J. Colloid Interface Sci.* 510 (2018) 20–31.
- D.-G. Kim, S.-O. Ko, Effects of thermal modification of a biochar on persulfate activation and mechanisms of catalytic degradation of a pharmaceutical, *Chem. Eng. J.* 399 (2020).
- Liang, L. Fu, Activation of peroxymonosulfate (PMS) by Co₃O₄ quantum dots decorated hierarchical C@Co₃O₄ for degradation of organic pollutants: kinetics and radical-nonradical cooperation mechanisms, *Appl. Surf. Sci.* 563 (2021).
- X.-l. Zou, H. Yan, X.-h. Chen, Evolution of second phases and mechanical properties of 7075 Al alloy processed by solution heat treatment, *Trans. Nonferrous Met. Soc. China* 27 (10) (2017) 2146–2155.
- Hu, et al., Activation of Na₂S₂O₈ by MIL-101(Fe)/Co₃O₄ composite for degrading tetracycline with visible light assistance, *Inorg. Chem. Commun.* 144 (2022).
- M.B. Asif, H. Kang, Z. Zhang, Gravity-driven layered double hydroxide nanosheet membrane activated peroxymonosulfate system for micropollutant degradation, *J. Hazard. Mater.* 425 (2022) 127988.
- Zhou, et al., Co₃O₄ anchored on biochar derived from chitosan (Co₃O₄@BCC) as a catalyst to efficiently activate peroxymonosulfate (PMS) for degradation of phenacetin, *J. Environ. Manag.* 327 (2023) 116895.
- Duan, et al., Unveiling the active sites of graphene-catalyzed peroxymonosulfate activation, *Carbon* 107 (2016) 371–378.

- [47] R.S. Ribeiro, et al., Magnetic carbon xerogels for the catalytic wet peroxide oxidation of sulfamethoxazole in environmentally relevant water matrices, *Appl. Catal. B: Environ.* 199 (2016) 170–186.
- [48] L. Liang, et al., Sucrose-derived N-doped carbon xerogels as efficient peroxydisulfate activators for non-radical degradation of organic pollutants, *J. Colloid Interface Sci.* 604 (2021) 660–669.
- [49] Y. Jo, et al., Activation of peroxymonosulfate on visible light irradiated TiO₂ via a charge transfer complex path, *Chem. Eng. J.* 346 (2018) 249–257.
- [50] W. Tian, et al., Enhanced removals of micropollutants in binary organic systems by biomass derived porous carbon/peroxymonosulfate, *J. Hazard. Mater.* 408 (2021) 124459.
- [51] A.H. Asif, et al., Heterogeneous activation of peroxymonosulfate by Co-doped Fe(2) O(3) nanospheres for degradation of p-hydroxybenzoic acid, *J. Colloid Interface Sci.* 604 (2021) 390–401.
- [52] W. Duan, et al., A unique Si-doped carbon nanocatalyst for peroxymonosulfate (PMS) activation: insights into the singlet oxygen generation mechanism and the abnormal salt effect, *Environ. Sci.: Nano* 7 (10) (2020) 2982–2994.
- [53] P. Liang, et al., An insight into metal organic framework derived N-doped graphene for the oxidative degradation of persistent contaminants: formation mechanism and generation of singlet oxygen from peroxymonosulfate, *Environ. Sci.: Nano* 4 (2) (2017) 315–324.
- [54] M.B. Asif, H. Kang, Z. Zhang, Assembling CoAl-layered metal oxide into the gravity-driven catalytic membrane for Fenton-like catalytic degradation of pharmaceuticals and personal care products, *Chem. Eng. J.* 463 (2023).
- [55] A.B. Grommet, M. Feller, R. Klajn, Chemical reactivity under nanoconfinement, *Nat. Nanotechnol.* 15 (4) (2020) 256–271.
- [56] C. Meng, et al., Laminar membranes assembled by ultrathin cobalt-copper oxide nanosheets for nanoconfined catalytic degradation of contaminants, *Chem. Eng. J.* 449 (2022).
- [57] R. Mu, et al., Functionally-designed metal salt and ball milling co-modified sludge biochar for adsorptive removal of trace level sulfamethoxazole: behavior, characterization, mechanism and DFT study, *J. Environ. Chem. Eng.* 12 (5) (2024).
- [58] E. Lorenc-Grabowska, Effect of micropore size distribution on phenol adsorption on steam activated carbons, *Adsorption* 22 (4-6) (2015) 599–607.
- [59] Z. Wang, et al., Honeycomb-like holey Co(3)O(4) membrane triggered peroxymonosulfate activation for rapid degradation of organic contaminants, *Sci. Total Environ.* 814 (2022) 152698.
- [60] J.-C.E. Yang, et al., Novel magnetic rod-like Mn-Fe oxycarbide toward peroxymonosulfate activation for efficient oxidation of butyl paraben: radical oxidation versus singlet oxygenation, *Appl. Catal. B: Environ.* (2020) 268.
- [61] J.-C.E. Yang, et al., The mechanistic difference of 1T-2H MoS₂ homojunctions in persulfates activation: structure-dependent oxidation pathways, *Appl. Catal. B: Environ.* 297 (2021).
- [62] X. Hu, M. Zhu, Were persulfate-based advanced oxidation processes really understood? Basic concepts, cognitive biases, and experimental details, *Environ. Sci. Technol.* 58 (24) (2024) 10415–10444.
- [63] J.-C.E. Yang, et al., Novel magnetic rod-like Mn-Fe oxycarbide toward peroxymonosulfate activation for efficient oxidation of butyl paraben: radical oxidation versus singlet oxygenation, *Appl. Catal. B: Environ.* 268 (2020) 118549.
- [64] J. Ye, et al., Synergy of pore confinement and co-catalytic effects in peroxymonosulfate activation for persistent and selective removal of contaminants, *Chem. Eng. J.* 496 (2024).
- [65] X. Shi, et al., Co and N co-doped carbon nanotubes catalyst for PMS activation: role of non-radicals, *Sep. Purif. Technol.* 353 (2025).
- [66] D.S. Sholl, R.P. Lively, Seven chemical separations to change the world, *Nature* 532 (7600) (2016) 435–437.